An Adaptive Phase Optimization Algorithm for Distributed Scatterer Phase History Retrieval

Shijin Li ⬤, Shubi Zhang, Tao Li, Yandong Gao ⬤, Qianfu Chen, and Xiang Zhang

Abstract—The multitemporal interferometric synthetic aperture radar (InSAR) technique based on distributed scatterers (DSs) has been widely applied in high-precision deformation measurements, which compensates for the drawback that the persistent scatterer InSAR technique does not obtain sufficient monitoring points, especially in rural areas. Considering that DS pixels are susceptible to various decorrelation factors, it is necessary to retrieve the optimal phase series by phase optimization algorithms (POAs). However, conventional POAs rely on a sample covariance matrix or complex coherence matrix (CCM) derived by spatially averaging statistically homogeneous pixel neighborhoods, which may blur and destroy phase information, especially in dense fringe areas. To overcome this limitation, an adaptive POA is proposed in this article. The adaptive POA artificially constructs a superior CCM by the filtered interferometric phase, which is derived through spatial adaptive filtering approach fusion of principal phase component estimation and fast nonlocal means filtering, and an accurate coherence matrix determined via coherence estimation bias correction. Moreover, the modified eigen-decomposition-based maximum-likelihood-estimator of the interferometric phase (EMI) with coherence-power-weighting is proposed to further improve the estimation precision and computational efficiency. The estimated CCM is then processed with the modified coherence-power-weighted EMI algorithm, and the optimal phase history is retrieved. The experimental results validated against both simulated and Sentinel-1A data demonstrate the superior optimization performance and robustness of the adaptive POA over traditional POAs.

Index Terms—Complex coherence matrix (CCM), distributed scatterer (DS), interferometric synthetic aperture radar (InSAR), phase history, spatial adaptive filtering.

I. INTRODUCTION

DIFFERENTIAL interferometric synthetic aperture radar (DInSAR) is a useful microwave remote sensing technique

that facilitates the measurement of ground deformation at the centimeter to millimeter accuracy [1]. Its effectiveness and recognition ability have been proven by its wide application in urban infrastructure [2], mining [3], earthquake monitoring [4], landslide research [5], volcanic activity assessment [6], etc. However, DInSAR results are usually contaminated by temporal and geometrical decorrelation due to the reflectivity changes and atmospheric perturbations resulting from time-varying tropospheric and ionospheric conditions. To overcome these limitations, multitemporal InSAR techniques using time series SAR scenes have been developed in recent decades. The initial popular persistent scatterer (PS) InSAR technique [7] derives high-precision surface deformation information by identifying PSs, which are pointwise deterministic objects exhibiting phase stability even over long time intervals and baseline separations. The density of PS pixels in urban areas is typically sufficient, whereas it is quite limited in rough terrains or nonurban regions. Subsequently, distributed scatterers (DSs) were introduced to improve the density of measurement points. In contrast to PS pixels with one dominant scatterer, DS pixels consist of multiple independent scatterers within a resolution cell. Hence, the phase quality corresponding to DSs is suboptimal and tends to exhibit temporal and geometrical decorrelation. To address this problem, an algorithm to extract information from DSs was developed using small baseline subsets (SBASs) [8]. SBAS techniques exploit differential interferograms with only short spatiotemporal baselines, and additional spectral or spatial filtering is employed to limit the decorrelation phenomena. Generally, these methods are at the cost of spatial resolution due to the straightforward rectangular estimation window [9]. Additionally, the multilooking process or nonlinear filtering approach may invalidate the phase consistency hypothesis [10], which is also called phase triangularity [11]. However, most coherence models for SAR interferometry purposes implicitly assume phase consistency; otherwise, this would challenge any simple interpretation of the interferometric phase [12].

In contrast to SBAS techniques, SqueeSAR [11] provides another way to reduce the decorrelation noise relative to DSs by retrieving the optimized phase history using all possible interferometric pairs. Furthermore, this method is based on the principle of phase consistency and theoretically decreases the estimation bias in the presence of phase inconsistency [12]. Specifically, SqueeSAR applies the phase triangulation algorithm (PTA) to the complex coherence matrix (CCM), which is estimated based on statistically homogeneous pixel (SHP) neighborhoods detected with the Kolmogorov–Smirnov test. The optimized phase

values of the selected DS pixels are then derived to replace the original SAR phase values, which are regarded as quasi-PS pixels jointly processed with PS pixels. Theoretically, the PTA is based on the maximization of the multivariate joint-probability distribution function (JPDF) of SHPs, which is similar to the phase linking algorithm [13], and the estimator should be the closest to the Cramér–Rao lower bound. However, the sample covariance or coherence matrix derived by the averaging of SHP neighborhoods is not robust against any type of outlier [14]. A single outlier in the samples, such as the heterogeneous pixels due to inaccurate SHP detection algorithms, could considerably bias the estimates. Furthermore, the coherence estimator is also limited by the number of samples [15]. Subsequently, robust estimation [14] and coherence bias correction [16]–[18] have been performed to improve the accuracy of systematic phase series retrieval. Additionally, researchers have also extended these kinds of methods, which are collectively referred to as phase optimization algorithms (POAs) in this article, by introducing eigenvalue decomposition (EVD). For instance, the Component extrAction and sElection SAR (CAESAR) [19] algorithm is based on covariance matrix decomposition, and the phase-decomposition-based PS InSAR (PD-PSInSAR) [20] algorithm is based on CCM decomposition. Note that EVD algorithms focus more on the tomographic separation of multiple scattering mechanisms, particularly with respect to the Rayleigh resolution. In terms of phase series optimization, the PTA or improved PTA outperforms EVD algorithms [21], [22].

Although the above methods adopt different strategies to reduce the decorrelation of DS pixels, these estimators share a similar mathematical model [23], [24]. The fundamental difference among these estimators is that they assign different weight factors to the interferometric observations. On the basis of the generic form, the authors introduce two modified PTAs, i.e., the equal- and coherence-weighted PTAs [24], [25]. In particular, the PTA and improved PTA are associated with the nonlinear optimization problem, and the optimal solution is derived through iterative analysis. Advanced studies have revealed that the Broyden–Fletcher–Goldfarb–Shanno (BFGS) method achieves a good performance in phase optimization [26]. However, it remains a time-consuming approach, which is sensitive to the initial phase value [27]. In pioneering studies, this limitation has been eased by the eigen-decomposition-based maximum-likelihood-estimator of the interferometric phase (EMI) [27] algorithm, and the EMI algorithm slightly reduces the impact of the coherence estimation error on phase estimation. Furthermore, the authors also introduce a sequential estimator adapted to high-precision near-real-time InSAR processing. Undeniably, other improved algorithms also attain a good performance in practical time series monitoring applications [5], [28], [29].

Evidently, the aforementioned POAs all involve analysis of the covariance matrix, which contains the coherence and phase information of all possible interferometric pairs. Generally, the sample covariance matrix is only estimated with the spatial multilook approach targeting the SHP neighborhood. This nonrobust estimation method raises two limitations in regard to phase optimization processing. One is that the coherence estimation is bias, and it has been mentioned above. The other is that the

phase filtering is not adaptive. Although the spatial filtering process is based on the SHP neighborhood, SHP selection usually only utilizes amplitude information. That is, the SHP selection method relies on the assumption that the amplitude value of pixels can also be regarded as an indication of the changes in their phase values [30], [31]; however, this is not the case. Especially for those interferometric pairs with dense fringes due to large deformation, which may be caused by a high deformation rate or long time interval, spatial multilooking may potentially cause blurring or even the loss of phase information.

This article, therefore, proposes an adaptive POA for the retrieval of the optimal phase history by fusing spatial adaptive filtering and modified EMI algorithm with coherence-power-weighting. The proposed approach first introduces a spatial adaptive interferogram filtering method combining principal phase component extraction and fast nonlocal mean filtering. Coherence estimation based on the filtered phase and SHP neighborhood and coherence bias correction based on the second kind statistical characteristic are thereafter performed. A more accurate CCM can then be derived. Subsequently, the modified coherence-power-weighted EMI algorithm is applied to the estimated CCM, and the optimized phase series is obtained. This proposed approach is validated against both simulated and Sentinel-1A real data.

This article is organized as follows. Section II reviews the theoretical basis of the traditional POA and describes the modified coherence-power-weighted EMI algorithm. In Section III, the proposed adaptive POA is elaborated, which contains the spatial adaptive filtering method, accurate CCM estimation and application of the modified EMI algorithm. Sections IV and V describe the experimental results compared to those acquired with *state-of-the-art* POAs using simulated and Sentinel-1A real data, respectively. In Section VI, a discussion on the experimental results processed by the modified EMI algorithm under the traditional CCM estimator is provided. Finally, conclusion is outlined in Section VII.

II. Modified Coherence-Power-Weighted EMI Algorithm

A. Statistical Properties of SAR Images

The covariance matrix, which statistically characterizes DS pixels, is the basis of all POAs. In addition, it is usually nonrobustly estimated as follows:

$$\hat{\mathbf{C}} = \frac{1}{N_{\text{SHP}}} \sum_{\mathbf{x} \in \Omega} \mathbf{x}\mathbf{x}^H \tag{1}$$

where $\hat{\mathbf{C}}$ is the sample covariance matrix, N_{SHP} is the number of pixels in SHP neighborhood Ω, $\mathbf{x}$ is the $N \times 1$ vector containing the original complex observations of the SAR images, N is the number of SAR images, and $(\cdot)^H$ is the conjugate transpose operation. However, to avoid the influence of the unbalanced backscattered power among the SAR images, the CCM usually replaces the sample covariance matrix [11]. Similarly, the CCM

is derived as

$$\hat{\mathbf{T}} = \frac{\hat{\mathbf{C}}}{\sigma\sigma^T} = \frac{1}{N_{\text{SHP}}} \sum_{\mathbf{y} \in \Omega} \mathbf{y}\mathbf{y}^H \tag{2}$$

where σ is the $N \times 1$ vector containing the standard deviations of the data with $\sigma_i = \sqrt{E[|x_i|^2]}$, and $\mathbf{y}$ are the normalized complex observations from $\mathbf{x}$, i.e., $y_i = x_i/\sqrt{E[|x_i|^2]}$. Note that the division operation of the middle term in (2) is an elementwise operation. Furthermore, the CCM can be described by the coherence matrix $|\hat{\mathbf{T}}|$ and interferometric phase matrix $\mathbf{\Phi}$ as follows:

$$\hat{\mathbf{T}} = |\hat{\mathbf{T}}| \circ \mathbf{\Phi} \tag{3}$$

with $\mathbf{\Phi} = \exp(j\varphi_{m,n})$, where $\varphi_{m,n}$ is the interferometric phase between the mth and nth acquisitions, $|\cdot|$ is the elementwise absolute value of the matrix, and $\circ$ is the Hadamard product.

B. Phase Triangulation Algorithm and EMI

Initially, the optimized phase is derived by maximizing the JPDF of the SHP neighborhood or maximizing the absolute value of the logarithm of this JPDF as follows:

$$\hat{\mathbf{\Sigma}} = \arg \max_{\mathbf{\Sigma}} \{\ln[p(\hat{\mathbf{T}}|\mathbf{\Sigma})]\}$$
$$= \arg \max_{\mathbf{\Sigma}} \left\{ tr(-\mathbf{\Sigma}^{-1}\hat{\mathbf{T}}) - \ln(Det(\mathbf{\Sigma})) \right\}, \tag{4}$$

where $tr(\cdot)$ is the trace of the matrix, $Det(\cdot)$ is the matrix determinant, and Σ is introduced as a model of the underlying covariance of an n-variate complex circular Gaussian process [27]. Generally, the above is expressed using the true coherence values and true phase values as follows:

$$\mathbf{\Sigma} = \psi\gamma\psi^H = \boldsymbol{\gamma} \circ \boldsymbol{\theta}\boldsymbol{\theta}^H$$
$$\psi = \text{diag}[\boldsymbol{\theta}] = \text{diag}[\exp(j\theta_i)] \tag{5}$$

where $\boldsymbol{\gamma}$ is the $N \times N$ true coherence matrix, and $\boldsymbol{\theta}$ is the $N \times 1$ true phase vector of the SAR images, i.e., the optimized phase vector to be estimated.

Evidently, to estimate $\boldsymbol{\theta}$, $\boldsymbol{\gamma}$ is required. The PTA and EMI all replace it with the estimated coherence matrix, i.e., $\gamma = |\hat{\mathbf{T}}|$.

However, in contrast to the PTA, the EMI algorithm introduces two scaling parameters

$$\psi' = \alpha \text{ diag}[\mathbf{\Theta}] = \alpha \text{ diag}[\eta_i \exp(j\theta_i)]$$
$$\mathbf{\Sigma} = \psi'\gamma\psi'^H = \alpha^2\boldsymbol{\gamma} \circ \boldsymbol{\eta}\boldsymbol{\eta}^H \circ \boldsymbol{\theta}\boldsymbol{\theta}^H \tag{6}$$

which provides extra freedom for the calibration of $|\hat{\mathbf{T}}|$ [27]. This introduction provides a possibility of calibration when the estimation of the coherence matrix is erroneous. Otherwise, the EMI algorithm equals the PTA when the coherence estimation error is absent, i.e., $\alpha^2 = 1$ and $\eta = \tilde{\mathbf{1}}$. Although the calibration effectiveness afforded by the two scaling parameters is slight, EMI attains a high computational efficiency by utilizing the Lagrange multiplier method to approximate and constrain model (4) under condition (6).

Note that the optimized phases of the PTA and EMI are all relative, meaning that the phase of an arbitrary image is set to 0, and the remaining phases are derived relative to this image.

C. Modified Coherence-Power-Weighted EMI Algorithm

Esfahany [23] and Ning *et al.* [24], respectively, derived a generic mathematical model through systematic analysis of existing POAs, such as the PTA, CAESAR, and PD-PSInSAR. Theoretically, the two models are equal, which is expressed as

$$\hat{\theta} = \arg \max_{\boldsymbol{\theta}} \left\{ \boldsymbol{\theta}^H(\mathbf{w} \circ \mathbf{\Phi})\boldsymbol{\theta} \right\}$$
$$= \arg \max_{\boldsymbol{\theta}} \left\{ \sum_{m=1}^{N} \sum_{n>m}^{N} w_{m,n} \cos(\varphi_{m,n} - \theta_{m,n}) \right\} \tag{7}$$

with $\theta_{m,n} = \theta_m - \theta_n$, where w is the weight factor of the residual phase, which is the only difference among the aforementioned POAs. In regard to the PTA, $\mathbf{w}_{\text{PTA}} = -|\hat{\mathbf{T}}|^{-1} \circ |\hat{\mathbf{T}}|$. Moreover, on the basis of the weight value difference, modified PTAs with equal-weighted $\mathbf{w}_{\text{Equal}} = \mathbf{J}$, i.e., all-ones matrix, and coherence-weighted $\mathbf{w}_{\text{Coh}} = |\hat{\mathbf{T}}|$ have also been proposed [24]. Actually, the two weighting methods can be expressed in the generic form of the power in regard to coherence, as previously reported [32]

$$\mathbf{w}_{\text{Coh}-P} = |\hat{\mathbf{T}}|^{\circ\,k}. \tag{8}$$

Note that the power k operation here occurs elementwise. It represents the equal-weighted PTA as $k = 0$ and the coherence-weighted PTA as $k = 1$. Certainly, k may also equal other real positive numbers, and [32] empirically demonstrated that the coherence-power-weighted model achieves good results at a k value of 1 or 2.

Substituting (8) into (7), the following is obtained

$$\hat{\theta} = \arg \max_{\theta} \left\{ \boldsymbol{\theta}^H(\mathbf{w}_{Coh-P} \circ \mathbf{\Phi})\boldsymbol{\theta} \right\}$$
$$= \arg \max_{\theta} \left\{ \boldsymbol{\theta}^H(|\hat{\mathbf{T}}|^{\circ\,(k-1)} \circ \hat{\mathbf{T}})\boldsymbol{\theta} \right\}. \tag{9}$$

Similar to the PTA, (9) can also be derived by (4) under the condition $\psi = \text{diag}[\theta] = \text{diag}[\exp(j\theta_i)]$, i.e.,

$$\hat{\mathbf{\Sigma}} = \arg \max_{\mathbf{\Sigma}} \left\{ tr(-\mathbf{\Sigma}^{-1}\hat{\mathbf{T}}) - \ln(Det(\mathbf{\Sigma})) \right\}$$
$$= \arg \max_{\gamma,\theta} \left\{ tr(-\psi\gamma^{-1}\psi^H\hat{\mathbf{T}}) - \ln(Det(\boldsymbol{\gamma})) \right\} \tag{10}$$
$$= \arg \max_{\theta} \left\{ \boldsymbol{\theta}^H(-\hat{\gamma}^{-1} \circ \hat{\mathbf{T}})\boldsymbol{\theta} \right\}$$

with $\hat{\gamma} = -[|\hat{\mathbf{T}}|^{\circ(k-1)}]^{-1}$. It is found that the difference between the PTA and modified coherence-power-weighted PTA only involves the variables adopted to replace γ.

Interestingly, the scaling parameters introduced by EMI only act on ψ, which is also the difference between the PTA and EMI, which does not involve γ. Therefore, the modified coherence-power-weighted EMI algorithm is derived as

$$\psi' = \alpha \text{ diag}[\mathbf{\Theta}] = \alpha \text{ diag}[\eta_i \exp(j\theta_i)]$$
$$\mathbf{\Sigma} = \psi'\hat{\gamma}\psi'^H = \alpha^2\hat{\gamma} \circ \boldsymbol{\eta}\boldsymbol{\eta}^H \circ \boldsymbol{\theta}\boldsymbol{\theta}^H$$
$$= -\alpha^2\left[|\hat{\mathbf{T}}|^{\circ\,(k-1)}\right]^{-1} \circ \boldsymbol{\eta}\boldsymbol{\eta}^H \circ \boldsymbol{\theta}\boldsymbol{\theta}^H. \tag{11}$$

Moreover, the method of the Lagrange multiplier in the EMI algorithm is not affected by γ, and it can also be employed to solve the modified coherence-power-weighted EMI algorithm. That is, the solution of the modified coherence-power-weighted

EMI is the minimum eigenvector of the Hadamard product $-|\hat{\mathbf{T}}|^{\circ(k-1)} \circ \hat{\mathbf{T}}$.

III. ADAPTIVE POA

At present, the proposed POAs all involve the sample covariance matrix or CCM, which is estimated by (1) or (2), respectively, and they contain the coherence and phase information of all possible interferometric pairs. In terms of the coherence, it is usually bias due to insufficient samples [15] and the presence of heterogeneous pixels in the SHP neighborhood caused by inaccurate estimation. However, we find that the estimated coherence usually acts on the weighting factor in the generic mathematical model (7). Robust coherence estimation [14], [16]–[18] and different weight settings [24], [28] have been widely studied to decrease the influence of the estimation bias.

In terms of the interferometric phase, the estimated phase is spatially filtered by the SHP neighborhood. However, SHPs are always selected based on the amplitude information of the SAR images. If an object in the scene causes a backscattering amplitude similar to that of the background, its phase will be mixed with that of the background during filtering, potentially causing blurring or loss of phase fringe information [31]. Extremely, for mine monitoring with a high deformation rate, the interferometric phase at moderate or long temporal intervals is basically independent of the amplitude information. In other words, the main phase component caused by deformation does not rely on the amplitude. In this case, the dense fringes are easily damaged by the spatial average, which leads to phase information loss. Hence, the estimated phase derived by (3) is suboptimal.

Here, we propose an adaptive POA fusion of spatial adaptive filtering and the modified coherence-power-weighted EMI algorithm.

A. Spatial Adaptive Filtering

Over the past two decades, a large number of adaptive filtering methods [33], [34] has been proposed based on the spatial and frequency domains to balance phase noise suppression and phase fringe information preservation. On the basis of previous studies [35], we propose an efficient and effective adaptive filtering method by combining principal phase component estimation and fast nonlocal means filtering.

The interferogram power spectrum is characterized by a narrow-band component corresponding to the phase information and a broadband noise component. Therefore, the principal phase component corresponding to the dominant frequency spectrum can be estimated with a reasonable threshold in the frequency domain

$$S_{(u,v)} = \text{FFT2}\left\{\phi_{(m,n)}\right\}$$
$$\phi'_{(m,n)} = \text{FFT2}^{-1}\left\{S_{(u,v)} \circ S^M_{(u,v)}\right\} \quad (12)$$

where $\phi_{(m,n)}$ and $\phi'_{(m,n)}$ are the original and filtered local phase patches, respectively, centered on the pixel in row m and column n, $\text{FFT2}\{\cdot\}$ is the 2-D fast Fourier transformation operation, and $S_{(u,v)}$ and $S^M_{(u,v)}$ are the frequency spectrum and dominant

frequency spectrum amplitude, respectively, for this patch. The latter is derived by the following rule [36]

$$S^M_{(u,v)} = \begin{cases} |S_{(u,v)}| & , \quad S_{(u,v)} \geq \text{thr} \\ 0 & , \quad S_{(u,v)} < \text{thr} \end{cases} \quad (13)$$

with $\text{thr} = \max(|S_{(u,v)}|)/\sqrt{2}$. The central pixel value of $\phi'_{(m,n)}$ is regarded as the filtered phase in row m and column n, and the filtered interferogram $\tilde{\phi}_M$ is obtained by elementwise traversal.

The size of the local patch in frequency analysis (12) greatly affects the strength of filtering, which may result in either under- or overfiltering. Therefore, the adaptive window size estimation method proposed in a previous study [35] is applied in the process of principal phase component estimation

$$N = \left\lfloor \sqrt{\frac{1}{2\varepsilon_0^2} \frac{1-r^2}{r^2}} \right\rfloor \quad (14)$$

where N is the size of the square window, $\lfloor \cdot \rfloor$ is the rounding operation, r is the coherence coefficient of the phase to be filtered, and ε is the standard deviation of the phase noise.

Furthermore, the fast nonlocal means filtering proposed in a previous study [33] is performed for the residual noise, which equals $\phi_R = \phi - \tilde{\phi}_M$, to save the residual phase information.

Eventually, the final filtered interferogram is derived as follows:

$$\tilde{\phi} = \tilde{\phi}_M + \tilde{\phi}_R \quad (15)$$

where $\tilde{\phi}_M$ are the filtered results obtained by principal phase component estimation and $\tilde{\phi}_R$ are the filtered results obtained by fast nonlocal means filtering.

B. CCM Estimation

To reduce the influence of the nonstationarity of SAR image signals on coherence estimation, the fast SHP selection (FaSHPS) algorithm [37] is adopted to determine SHP neighborhood Ω. Moreover, the interferometric phase after topography phase removal is used to decrease the effect of the nonstationarity of phase signals. Therefore, for reference pixel p, the coherence corresponding to the filtered interferometric phase is estimated by

$$\hat{\gamma}_p = \frac{\sum_{i \in \Omega} |s_1(i)||s_2(i)| \exp(j\tilde{\phi}(i))}{\sqrt{\sum_{i \in \Omega} |s_1(i)|^2 \sum_{i \in \Omega} |s_2(i)|^2}}, \quad (16)$$

where s_1 and s_2 are the complex SAR images. Inevitably, the estimated coherence is a biased estimator, especially for low coherence values.

Therefore, the second kind statistics defined with the Mellin transform (log-moment) [38] is applied to correct the above biased estimator

$$\tilde{\gamma} = \exp\left(\frac{1}{N_{\text{SHP}}} \sum_{i \in \Omega} \ln(\hat{\gamma}_i)\right) \quad (17)$$

where $\tilde{\gamma}$ is the corrected coherence estimator, namely, the final coherence matrix.

Once the filtered phase and corresponding coherence of all possible interferometric pairs, i.e., $N(N-1)/2$, have been

TABLE I
PSEUDOCODE OF THE ADAPTIVE POA PROCEDURE

Input Data: Time series SAR images
1. $\Omega \leftarrow$ Calculate the SHP neighborhood with the FaSHPS algorithm based on time series amplitude images;
2. *Network* $\leftarrow$ Set up a network containing all possible interferometric pairs;
for each interferogram $\in$ *Network* *do*
3. $\widetilde{\phi} \leftarrow$ Filter the original interferogram by the spatial adaptive filtering approach described in Section III-A;
4. $\hat{\gamma} \leftarrow$ Estimate the coherence matrix corresponding to the filtered interferogram $\widetilde{\phi}$ with (16);
5. $\widetilde{\gamma} \leftarrow$ Correct the coherence estimation bias using the second kind statistics described in (17);
end for
for each pixel $\in$ image *do*
6. $\widetilde{\gamma}'$, $\widetilde{\phi}' \leftarrow$ Extract the $N \times N$ matrix for the pixel to be processed from all possible interferometric results $\widetilde{\gamma}$ and $\widetilde{\phi}$;
7. $\widetilde{\mathbf{T}} \leftarrow$ Construct the sample CCM with (18);
8. $\hat{\theta} \leftarrow$ Retrieve the optimal phase series by the modified coherence-power-weighted EMI algorithm, i.e., the minimum eigenvector of the Hadamard product $-\lvert\hat{\mathbf{T}}\rvert^{\circ(k-1)} \circ \hat{\mathbf{T}}$;
end for
Output Data: Optimized time series SAR images.

estimated by (15) and (17), respectively, the estimated sample CCM is then derived as follows:

$$\tilde{\mathbf{T}} = \tilde{\gamma}' \circ \tilde{\phi}' \tag{18}$$

where $\tilde{\gamma}'$ and $\tilde{\phi}'$ are $N \times N$ matrices for the reference pixel, which contains the information on all possible interferometric pair, and the former is expressed as

$$\tilde{\gamma}' = \begin{bmatrix} \tilde{\gamma}_{1,1} & \tilde{\gamma}_{1,2} & \cdots & \tilde{\gamma}_{1,N} \\ \tilde{\gamma}_{2,1} & \tilde{\gamma}_{2,2} & \cdots & \tilde{\gamma}_{2,N} \\ \vdots & \vdots & \ddots & \vdots \\ \tilde{\gamma}_{N,1} & \tilde{\gamma}_{N,2} & \cdots & \tilde{\gamma}_{N,N} \end{bmatrix} \tag{19}$$

where $\tilde{\gamma}_{i,j}$ is the estimated coherence corresponding to the filtered interferometric phase between the ith and jth acquisitions.

C. Retrieving the Optimal Phase History

After the estimated CCM is obtained, the modified EMI algorithm with coherence-power-weighting described in Section II-C can then be applied to retrieve the optimal phase history.

The detailed process flow of the adaptive POA is given in Table I. Note that similar to the traditional POAs, the optimized phase series is relative to arbitrary SAR images. However, in contrast to the traditional POAs, the adaptive POA not only abates the loss of phase fringe information resulting from spatial multilooking by spatial adaptive filtering but also avoids any iterative and inversion operations via the modified coherence-power-weighted EMI algorithm.

IV. EXPERIMENTAL RESULTS WITH SIMULATED DATA

A. Effective Evaluation of the Modified Coherence-Power-Weighted EMI Algorithm

Considering that the difference between the modified coherence-power-weighted EMI algorithm and the traditional POAs mainly involves the weight factor in the estimation procedure, which is related to the sample coherence matrix. Therefore, a simple simulation without interferometric phase information is performed, namely, the phase components produced by the topography, atmosphere, and deformation are all set to zero. The true coherence matrix is simulated combined with the generic decorrelation model [27]

$$T_{i,j} = (T_0 - T_\infty) \exp(-\delta t_{i,j}/\tau) + T_\infty \tag{20}$$

where T_0 is the short-term decay, T_∞ is the long-term persistent coherence, δt is the repeat cycle of satellite, i.e., the minimum temporal baseline of any interferogram used in the simulation, and τ is a time constant of the decorrelation process. In this experiment, the parameters are set as follows: $T_0 = 0.8$; $T_\infty = 0.05$; $\delta t = 6$; and $\tau = 50$. On the basis of the true coherence matrix, 50 images each containing 100–300 SHPs are synthesized [39], which assumes the complex circular Gaussian statistic and spatial stationarity in the generation of the data stack.

The rootmean-square error (RMSE) of the optimized phase processed by the different POAs and SHPs is shown in Fig. 1. As previously described in Section II, the main difference between the coherence-power-weighted POA and the traditional POAs is the selection of γ. Hence, the simulated true coherence matrix is also employed to replace γ, which is referred to as the EMI with true coherence (EMI-TC). Evidently, the results produced by EMI-TC are always optimal under any condition because it represents an ideal case where the coherence is the optimum estimate. The performance of the PTA and EMI is basically the same. However, the computation efficiency of the EMI algorithm is much higher than that of the PTA. They are all superior to the modified EMI with $k = 0$, i.e., the equal-weighted EMI. The reason for this phenomenon is that the method assigns the same weight to phases with differing coherence levels. Compared to this approach, the modified EMI for $k = 1, 2,$ and 3 is more robust to decorrelation because it assigns a high weight to the phase with a high coherence. Among them, the RMSE corresponding to the modified EMI for $k = 1$ is similar to that of the EMI and PTA or even slightly lower. The modified EMI for $k = 2$ and $k = 3$ attains the optimal performance, which is basically consistent with the conclusion of [32].

Moreover, as revealed in Fig. 1(b) and (c), the RMSE obtained with the different POAs decreases with increasing number of SHPs and gradually approaches the result of EMI-TC. This occurs because the coherence estimation error decreases with increasing number of SHPs.

B. Effective Evaluation of the Adaptive POA

In contrast to the experiment described in Section IV-A, the adaptive POA also involves the adaptive filtering process for
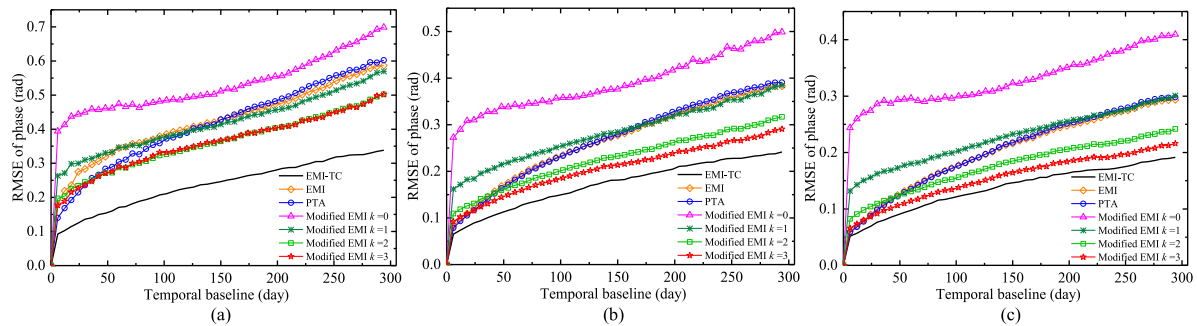
Fig. 1. Phase optimization results of the different POAs with distinct SHPs in the simulated case. EMI-TC is the EMI algorithm with the true coherence matrix. (a)–(c) represent 100, 200, and 300 SHPs, respectively.
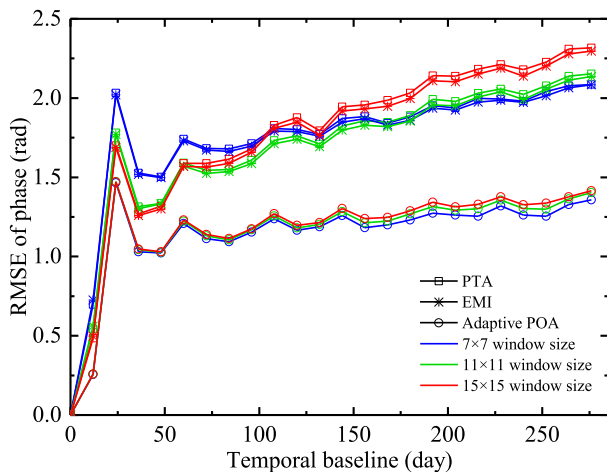

Fig. 2. Phase optimization results of the different POAs with the varying window sizes in SHP estimation in the simulated data containing a high deformation rate.

phase observation. Therefore, the interferometric phase information is simulated by supposing a circular subsidence funnel with a maximum settlement rate of 200 mm/year and a radar wavelength of 55 mm. The atmospheric and topographic phases are still neglected. The coherence is estimated using (20) with $T_0 = 0.8$, $T_\infty = 0.2$, $\delta t = 12$, and $\tau = 50$. Note that a large temporal interval and high deformation rate are adopted to more intuitively analyze the phase information loss under dense fringes. The amplitude information is contained in the real Sentinel-1A image of a suburban area, which references the location of deformation in the mining area. Eventually, a stack of 24 images with 128 pixels × 128 pixels is synthesized.

As described in Section IV-A, the modified coherence-power-weighted EMI algorithm performs better at $k = 2$ and $k = 3$. In view of this, $k = 2$ is adopted in the adaptive POA in this article. Then, the RMSE of the optimized phase series, obtained with the different POAs and window sizes in SHP estimation, are calculated to evaluate the reliability of the adaptive POA.

As shown in Fig. 2, regardless of the window size in SHP estimation, the PTA and EMI attain very similar results. This is consistent with the experimental conclusion described in Section IV-A. However, the difference is that the optimization effects of the PTA and EMI do not blindly increase with increasing number of SHPs. In terms of the first few images,

the RMSE of the optimized phase decreases with increasing number of SHPs. On the one hand, the coherence estimation bias gradually decreases with increasing number of SHPs. On the other hand, with increasing number of SHPs, the strength of spatial filtering dependent on (2) increases, indicating that noise suppression becomes more obvious and therefore yields a better optimized result. Nevertheless, for the later SAR images, which generate the interferometric phase under dense fringes due to the long temporal baseline, the optimized phase worsens with increasing number of SHPs. The main reason is that the phase is overfiltered due to the large number of SHPs and the nonadaptive filtering process of (2). This blurs and destroys the phase, especially in areas containing dense fringes, and further affects the performance of phase optimization. However, the adaptive POA always generates the optimal results, and the optimization effect with different numbers of SHPs basically remains consistent and optimal. Moreover, with increasing temporal baseline, the adaptive POA maintains the approximate performance, which further demonstrates the higher robustness than that of the PTA and EMI.

To intuitively analyze the advantages of the adaptive POA in phase fringe information preservation, the interferogram with the longest temporal baseline is selected as an example, and the processed results are shown in Fig. 3 . Theoretically, interferograms with long temporal baselines are expected to exhibit dense fringes and experience severe temporal decorrelation. Hence, the inspection of such interferograms will be more conclusive in terms of the examination of the merit of the applied POAs. In addition, considering the similar results produced by the PTA and EMI, the optimized interferogram processed by EMI is only shown. As shown in Fig. 3(e), although a large estimation window is adopted to improve the accuracy of coherence estimation, this also leads to spatial overfiltering, which does not recover phase detail information, especially underdense fringes. However, the adaptive POA considers both phase decorrelation suppression and phase information preservation and evidently performs well.

V. EXPERIMENTAL RESULTS WITH REAL DATA

The study area shown in Fig. 4 is located in Datong city, Shanxi Province, which is one of the largest coal energy bases in China and includes Permian–Carboniferous and Jurassic coalfields. However, in recent years, excessive exploitation of
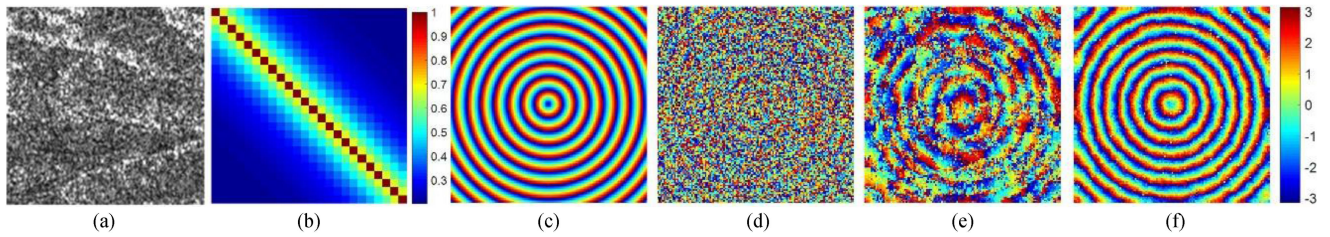
Fig. 3. Interferometric phase under the longest temporal baseline of 276 days. (a) Amplitude image. (b) Simulated true coherence matrix. (c) Simulated true phase. (d) Simulated original phase. (e) Optimized phase produced by EMI with a 15 × 15 window size in SHP estimation. (f) Optimized phase produced by the adaptive POA with a 15 × 15 window size in SHP estimation. Noted that, (c)–(f) share the same color bar.
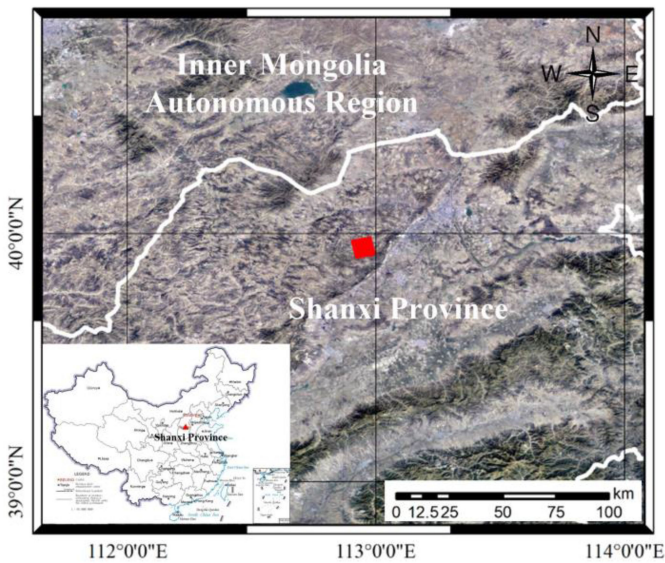

Fig. 4. Geographic location of the study area.

coal resources has led to serious surface subsidence, which has threatened people's lives and property.

To further verify the effectiveness of the adaptive POA, time series Sentinel-1A real data are used for experimental analysis. Specifically, 24 SAR scenes in the interferometric wide-swath mode and under vertical-vertical polarization acquired from September 24, 2019, to June 26, 2020, along an ascending orbit are processed. The experimental image size is 550 pixels × 1550 pixels, and the temporal interval is 12 days.

Similar to Section IV-B, $k = 2$ is also adopted in the modified coherence-power-weighted EMI algorithm during application of the adaptive POA, and window sizes of 15 × 15, 11 × 11, and 7 × 7 are applied in SHP estimation for a comparative analysis.

A. Visual Inspection

To evaluate the performance of the different POAs more intuitively, the interferogram of the long temporal baseline obtained by the optimized phase, which is more conclusive than the interferogram of the short temporal baseline, is analyzed via visual inspection. As shown in Fig. 5(a), the original interferometric phase suffers from serious decorrelation due to the long temporal baseline and volume scattering caused by the forest vegetation.

However, the POAs still effectively recover the necessary phase information because all interferometric pairs are utilized for the statistical analysis. That is, the $N(N-1)/2$ interferometric phase values are not redundant due to the spatial filtering process, which also confirms the necessity of spatial adaptive filtering. Fig. 5(b) and (c) reveals that the phase optimization effect realized by the PTA and EMI is approximate, and the phase fringe information is blurred, especially in the enlarged phase dense fringe area. In addition, it is difficult to determine the difference between them only by visual analysis. However, the interferometric phase obtained by the adaptive POA effectively recovers part of the phase information, and the phase fringe is not only continuous but also smooth. In view of the left area without an obvious phase change, the phase smoothing degree further demonstrates the superiority of the adaptive POA. Although the adaptive POA attains a higher performance than do the PTA and EMI, phase noise still occurs in the central region of the subsidence funnel. This phenomenon may be caused by significant decorrelation or excessive settlement, which may exceed the limit of InSAR deformation monitoring.

Additionally, we find that four main subsidence funnels are located in this study area, which are basically caused by over-exploitation in the coal mine.

B. Quantitative Assessment

Furthermore, a quantitative assessment of all possible interferograms obtained with the optimized phase is carried out to evaluate the reliability of the adaptive POA. In this article, the number of residues and the sum of the phase difference (SPD) [40] are considered as evaluation indexes to investigate the quality of the interferogram. Theoretically, the smaller the number of residues and SPD value are, the smoother the phase and the higher the phase quality are. Note that the performance evaluation with different window sizes in SHP estimation is only indicated by the mean value and standard deviation of the improvement percentage over the original interferogram.

As shown in Fig. 6(a), compared to the PTA and EMI, the number of residues corresponding to the adaptive POA is always the smallest, which demonstrates the effectiveness of the proposed approach in phase noise suppression. However, the treatment efficiency of the EMI algorithm is similar to that of the PTA, which is consistent with the conclusion drawn in Section IV. Interestingly, peaks occur in the intervals regardless of the POA
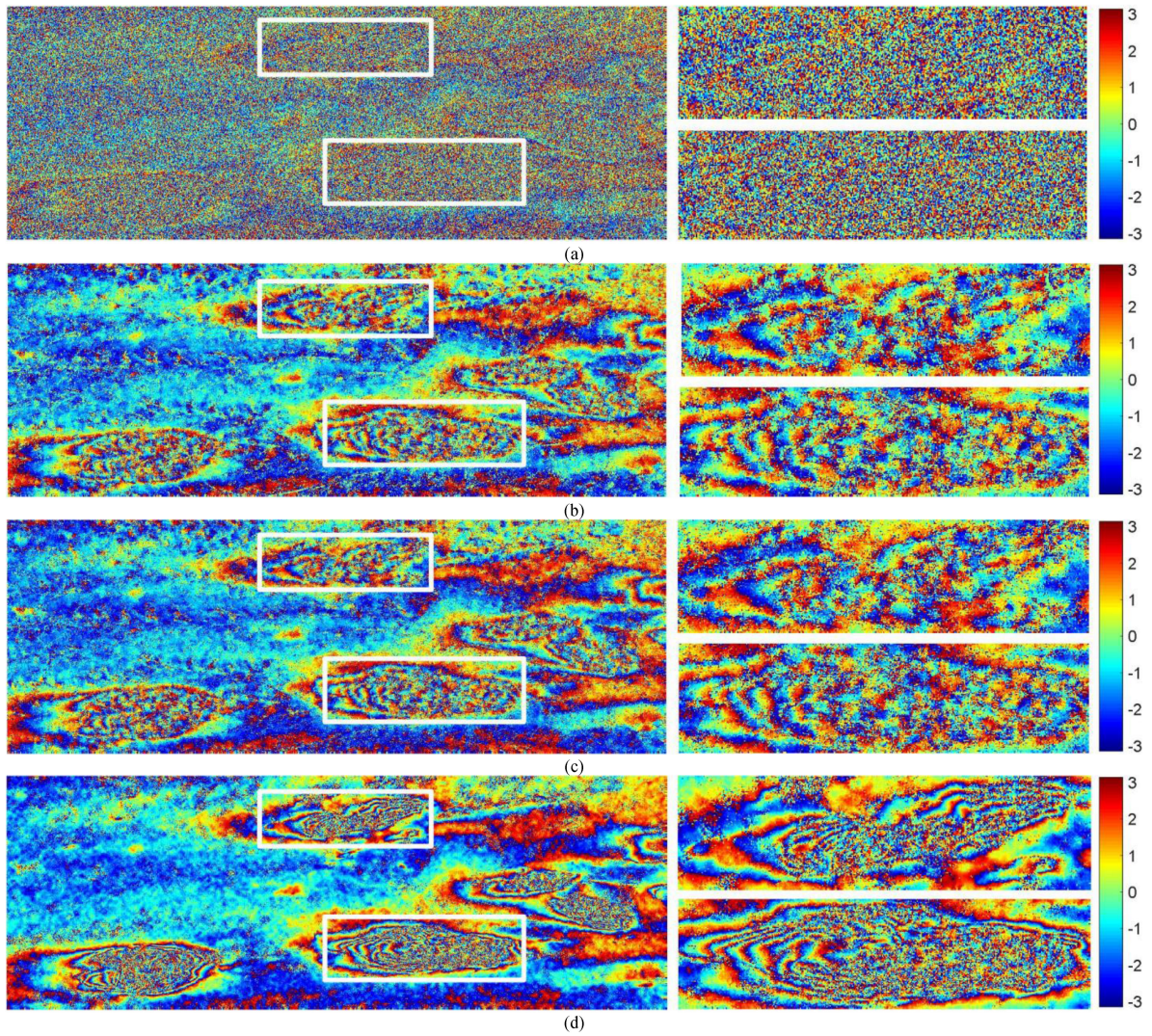
Fig. 5. Interferogram with a temporal baseline of 240 days obtained by the optimized phase. Note that the 15 × 15 window size is applied in SHP estimation. (a) Original interferogram. (b)–(d) Optimized interferograms processed by the PTA, EMI, and adaptive POA, respectively. The right column shows an enlarged display of the white box area in each image.
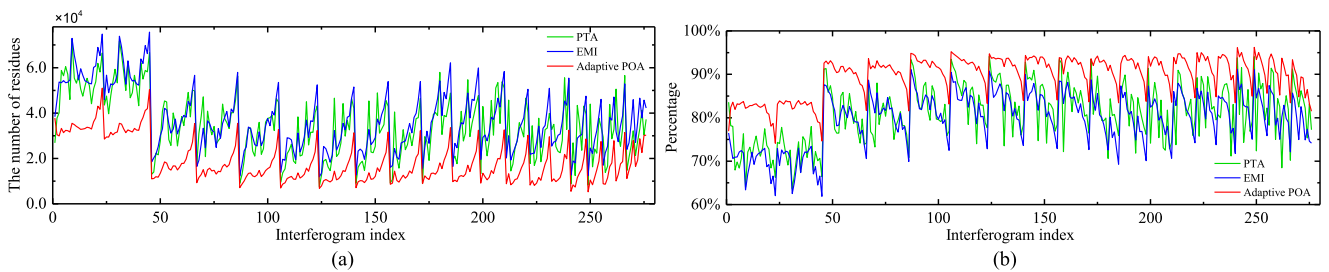

Fig. 6. Residues for all possible interferograms obtained with the optimized phase, as processed by the different POAs with the 15 × 15 SHP estimation window size. (a) Number of residues. (b) Improvement percentage over the original interferogram.

applied. In fact, a peak corresponds to the interferogram with the longest temporal baseline relative to each reference image. For this interferogram, the optimization performance of all POAs is not ideal. Through the improvement percentage over the original interferogram, it is found that the POAs all produce quite good phase noise suppression effects. The noise reduction rates of the PTA and EMI are basically consistent, and all are higher than

60%. Evidently, the noise reduction rate of the adaptive POA is much higher than that of the former algorithms, and the highest ratio reaches 95%. Conversely, troughs are observed in the intervals, as shown in Fig. 6(b). This indicates the low optimization performance of the long temporal baseline interferogram.

Based on the SPD values shown in Fig. 7, we draw the same conclusion. That is, compared to the original interferograms,
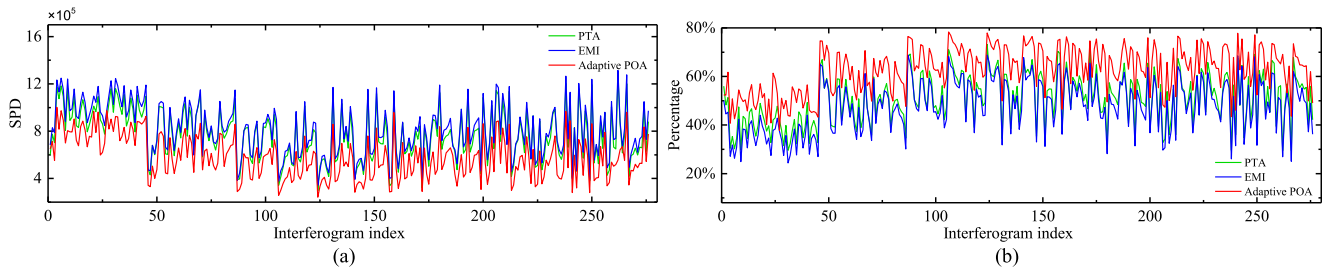
Fig. 7. SPD results for all possible interferograms obtained with the optimized phase, as processed by the different POAs with the 15 × 15 SHP estimation window size. (a) SPD values. (b) Improvement percentage over the original interferogram.
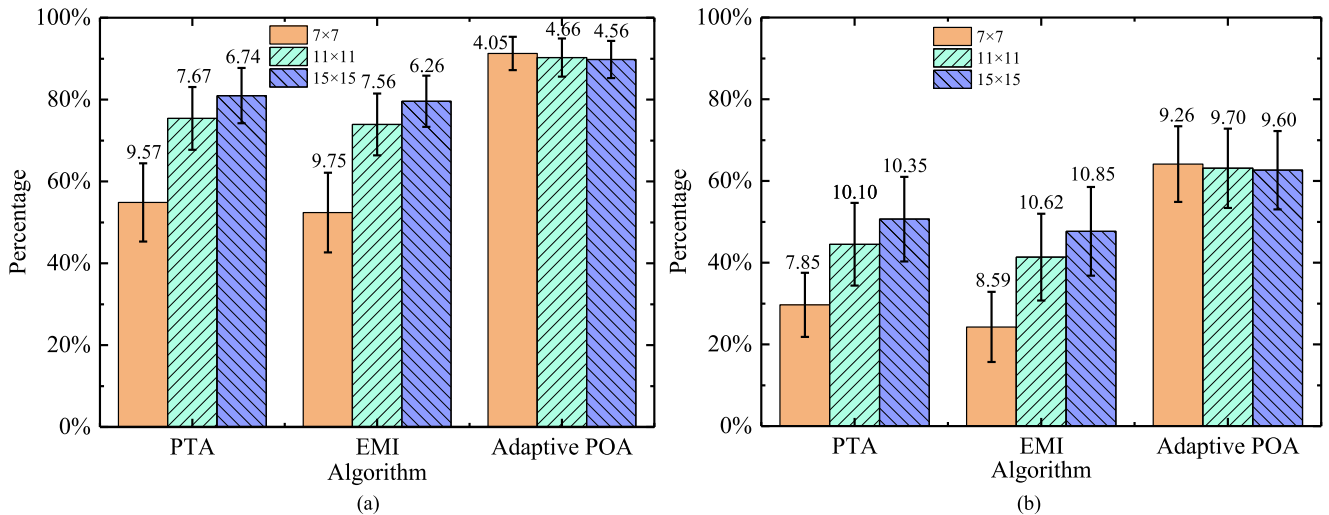

Fig. 8. Mean values and standard deviation of the improvement percentage obtained with the different POAs and SHP estimation window sizes. (a) Number of residues. (b) Sum of the phase difference.

all POAs exhibit good phase optimization results. Moreover, the optimized performance of the adaptive POA is significantly superior to that of the EMI and PTA, and that of the EMI algorithm is similar to that of the PTA. However, the difference is that the peaks and troughs shown in the SPD images of Fig. 7 are not as obvious as those shown in Fig. 6. This phenomenon may be caused by the varying performance of the evaluation index itself. Nevertheless, it is also found that the optimization effect of the POAs is relatively low for the long temporal baseline interferograms.

The mean value and standard deviation of the improvement percentage over the original interferogram in regard to the number of residues and SPD are further shown in Fig. 8. In terms of the same window size in SHP estimation, the larger mean value and smaller standard deviation indicate the greater improvement ability and higher robustness of the adaptive POA than those of the PTA and EMI, respectively. The overall performance of the PTA is similar to that of EMI, even slightly superior. With decreasing SHP estimation window size, the effectiveness and stability of the PTA and EMI greatly decrease due to inaccurate CCM estimation and poor spatial filtering. However, the optimization effect of the adaptive POA is rarely affected by the SHP estimation window size, which only acts on the coherence matrix estimation, and bias correction is performed later during

the proposed approach to reduce this effect. Of course, both the number of residues and SPD support the conclusion mentioned above, which verifies the effectiveness and stability of the adaptive POA.

C. Computational Time

Selecting the 15 × 15 window size in SHP estimation as an example, the cumulative process times of the different POAs for the real Sentinel-1A data are determined, as given Table II.

TABLE II
COMPUTATIONAL TIME FOR THE DIFFERENT POAs WITH A 15 × 15 SHP ESTIMATION WINDOW SIZE

POA	Process steps	Time (h)	Total time (h)
PTA	CCM estimation by (2)	0.126	6.272
	Solving (4) by BFGS under the condition (5)	6.146	
EMI	CCM estimation by (2)	0.126	0.337
	Solving (4) by EVD under the condition (6)	0.211	
Adaptive POA	Spatial adaptive filtering by (15)	3.064	4.104
	CCM estimation by (18)	0.974	
	Solving (4) by EVD under the condition (11)	0.066	

The POAs are conducted using MATLAB R2016b software with an Intel i7-9750H 2.60-GHz CPU and 16 GB of RAM. Noted that, the initialization during the process of solving (4) by BFGS adopts the minimum eigenvector of Hadamard product $\gamma^{-1} \circ \hat{\mathbf{T}}$ [27], and the maximum number of iterations is 4000.

As given in Table II, EMI obtains the highest computational efficiency, followed by the adaptive POA. Specifically, in terms of solving the optimized phase series, the time consumption of the adaptive POA and EMI is much lower than that of the PTA because the former methods do not require complex iterative processing. Moreover, although the same EVD solution strategy as that of EMI is adopted in the adaptive POA, the solution efficiency is obviously superior to that of EMI because the coherence-power-weighted approach does not require inversion operation. However, during the adaptive POA process, spatial adaptive filtering and CCM estimation are time-consuming steps because all possible interferometric pairs are processed. Nevertheless, the computational efficiency of the adaptive POA is superior to that of the PTA.

VI. Discussion

In previous studies, the quality of the phase series obtained by different POAs is usually assessed by the goodness-of-fit, which is expressed as [11]

$$\gamma_{\text{PTA}} = \frac{2}{N(N-1)} \text{Re} \left(\sum_{m=1}^{N} \sum_{n>m}^{N} \exp \left(j \left(\varphi_{m,n} - \hat{\theta}_{m,n} \right) \right) \right) \tag{21}$$

with $\hat{\theta}_{m,n} = \hat{\theta}_m - \hat{\theta}_n$, where $\hat{\theta}_i$ is the optimized phase series. However, the interferometric phase $\boldsymbol{\Phi}$ of the traditional POAs is derived by spatial filtering, as expressed in (1), namely, the goodness-of-fit index focuses more on the performance evaluation of the solution approach and weight factor in this case. Hence, for the adaptive POA using the different interferometric phases derived by (15), this quality index is not suitable for comparison with the PTA or EMI. Nevertheless, it may be adopted to further evaluate the effectiveness of the modified coherence-power-weighted EMI algorithm under the CCM estimator obtained with (1).

Selecting the same parameter $k = 2$ as adopted in the adaptive POA as an example, the modified coherence-power-weighted EMI algorithm is compared to the EMI algorithm under the condition of using the same CCM estimator derived by (1). Moreover, the Sentinel-1A data and 15×15 window size in SHP estimation are adopted. The experimental results are shown in Fig. 9.

Fig. 9(a) reveals that the phase fringe information is still blurred and destroyed, which is similar to the PTA and EMI results, as shown in Fig. 5(b) and (c), respectively. The reason for this phenomenon is that the estimated CCM obtained via nonadaptive spatial filtering is processed. Compared to the EMI algorithm, a better promotion effect in terms of the number of residues and SPD is obtained with the modified coherence-power-weighted EMI algorithm. Based on the mean value and standard deviation of the improvement percentage, as shown in Fig. 9(c), we demonstrate the superiority of the

modified coherence-power-weighted EMI algorithm more intuitively. However, they remain inferior to the adaptive POA. Furthermore, the goodness-of-fit of EMI and the modified coherence-power-weighted EMI algorithm are calculated with (21), and a comparison is shown in Fig. 9(d). It is found that the modified coherence-power-weighted EMI algorithm attains a higher goodness-of-fit than does EMI, i.e., it is slightly superior to the EMI algorithm. Additionally, the computational time is also recorded, which is 0.283 h. As mentioned in Section V-C, since the modified coherence-power-weighted EMI algorithm does not involve inversion operations, it is slightly more computationally efficient than EMI.

Generally, the performance of the modified coherence-power-weighted EMI algorithm is superior to that of the EMI algorithm, which is consistent with the conclusion presented in Section IV-A. However, it is inferior to the adaptive POA. The modified coherence-power-weighted EMI may have better application prospects in the absence of a high deformation rate, such as in urban health monitoring. And, this further reveals that the phase variation with large gradient has a great influence on the phase optimization process. If the large gradient phase variations could be removed by some approaches, such as the accurate settlement model, the modified coherence-power-weighted EMI algorithm or traditional POAs may have the excellent results.

VII. Conclusion

In this article, an adaptive POA for the retrieval of the optimal phase history is proposed, which combines the spatial adaptive filtering approach and modified coherence-power-weighted EMI algorithm. In contrast to traditional POAs, the sample CCM is artificially constructed with the filtered phase and accurate coherence matrix of all possible interferometric pairs, which are processed through spatial adaptive filtering and coherence estimation bias correction with the second kind statistics, respectively. This effectively avoids the blurring and destruction of phase information caused by SHP neighborhood averaging, especially in phase dense fringe areas. Moreover, the modified coherence-power-weighted EMI algorithm is applied for the estimated CCM to further improve the optimization results.

The experimental results with simulated and Sentinel-1A data all demonstrate the high optimization performance and robustness of the adaptive POA. Compared to the state-of-the-art techniques, the adaptive POA not only suppresses time series phase noise but also effectively preserves phase fringe detail information. Moreover, the adaptive POA does not require complex iteration and inversion operations. Noted that the computational efficiency of the adaptive POA is suboptimal because it separately processes all interferograms. And this is also the direction of further research.

Additionally, the effectiveness of the modified coherence-power-weighted EMI algorithm using the traditional CCM estimator is also demonstrated with both simulated and real data. In the presence of a slight deformation field, this method may have potential development prospects, which requires further research.
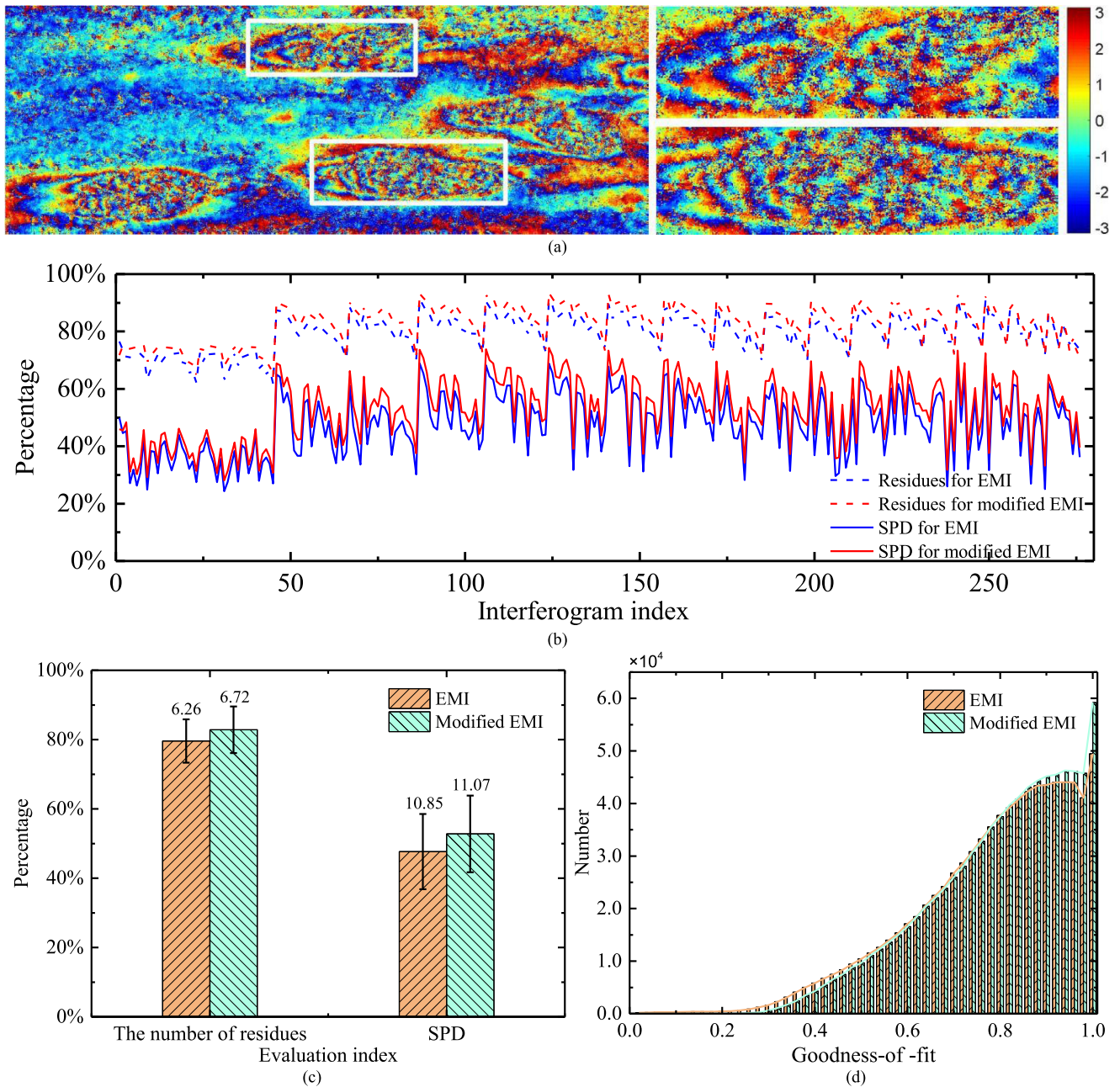
Fig. 9. Experimental results obtained with the modified coherence-power-weighted EMI algorithm. (a) Interferogram with a temporal baseline of 240 days obtained with the optimized phase. (b) Improvement percentage of the number of residues and SPD over the original interferogram. (c) Mean value and standard deviation of the improvement percentage. (d) Comparison of the histograms of goodness-of-fit.

ACKNOWLEDGMENT

REFERENCES

[1] F. Casu *et al.*, "SBAS-DInSAR parallel processing for deformation time-series computation," *IEEE J. Sel. Topics Appl. Earth Observ. Remote Sens.*, vol. 7, no. 8, pp. 3285–3296, Aug. 2014.

[2] Z. Zhang, C. Wang, M. Wang, Z. Wang, and H. Zhang, "Surface deformation monitoring in Zhengzhou city from 2014 to 2016 using time-series InSAR," *Remote Sens.*, vol. 10, no. 11, pp. 1731–1747, Nov. 2018.

[3] B. Chen *et al.*, "Three-dimensional time-varying large surface displacements in coal exploiting areas revealed through integration of SAR pixel offset measurements and mining subsidence model," *Remote Sens. Environ.*, vol. 240, 2020, Art. no. 111663.

[4] K. Materna *et al.*, "Source characteristics of the 2017 Mw6.4 moijabana, botswana earthquake, a rare lower-crustal event within an ancient zone of weakness," *Earth Planetary Sci. Lett.*, vol. 506, pp. 348–359, 2019.

[5] J. Dong *et al.*, "Mapping landslide surface displacements with time series SAR interferometry by combining persistent and distributed scatterers: A case study of Jiaju landslide in Danba, China," *Remote Sens. Environ.*, vol. 205, pp. 180–198, 2018.

[6] S. Vajedian, M. Motagh, and F. Nilfouroushan, "StaMPS improvement for deformation analysis in mountainous regions: Implications for the damavand volcano and Mosha fault in Alborz," *Remote Sens.*, vol. 7, no. 7, pp. 8323–8347, 2015.

[7] A. Ferretti, C. Prati, and F. Rocca, "Permanent scatterers in SAR interferometry," *IEEE Trans. Geosci. Remote Sens.*, vol. 39, no. 1, pp. 8–20, Jan. 2001.

[8] P. Berardino, G. Fornaro, R. Lanari, and E. Sansosti, "A new algorithm for surface deformation monitoring based on small baseline differential SAR interferograms," *IEEE Trans. Geosci. Remote Sens.*, vol. 40, no. 11, pp. 2375–2383, Nov. 2002.

[9] K. Goel, and N. Adam, "A distributed scatterer interferometry approach for precision monitoring of known surface deformation phenomena," *IEEE Trans. Geosci. Remote Sens.*, vol. 52, no. 9, pp. 5454–5468, Sep. 2014.

[10] F. Liu, and B. Pan, "A new 3-D minimum cost flow phase unwrapping algorithm based on closure phase," *IEEE Trans. Geosci. Remote Sens.*, vol. 58, no. 3, pp. 1857–1867, Mar. 2020.

[11] A. Ferretti, A. Fumagalli, F. Novali, C. Prati, F. Rocca, and A. Rucci, "A new algorithm for processing interferometric data-stacks: SqueeSAR," *IEEE Trans. Geosci. Remote Sens.*, vol. 49, no. 9, pp. 3460–3470, Sep. 2011.

[12] F. De Zan, M. Zonno, and P. Lopez-Dekker, "Phase inconsistencies and multiple scattering in SAR interferometry," *IEEE Trans. Geosci. Remote Sens.*, vol. 53, no. 12, pp. 6608–6616, Dec. 2015.

[13] A. M. Guarnieri, and S. Tebaldini, "On the exploitation of target statistics for SAR interferometry applications," *IEEE Trans. Geosci. Remote Sens.*, vol. 46, no. 11, pp. 3436–3443, Nov. 2008.

[14] Y. Wang, and X. X. Zhu, "Robust estimators for multipass SAR interferometry," *IEEE Trans. Geosci. Remote Sens.*, vol. 54, no. 2, pp. 968–980, Feb. 2016.

[15] M. Jiang, X. Ding, and Z. Li, "Hybrid approach for unbiased coherence estimation for multitemporal InSAR," *IEEE Trans. Geosci. Remote Sens.*, vol. 52, no. 5, pp. 2459–2473, May 2014.

[16] Z.-F. Ma, M. Jiang, and T. Huang, "A sequential approach for Sentinel-1 TOPS time-series co-registration over low coherence scenarios," *IEEE Trans. Geosci. Remote Sens.*, to be published, doi: 10.1109/TGRS.2020.3009996.

[17] Z.-F. Ma, M. Jiang, Y. Zhao, R. Malhotra, and B. Yong, "Minimum spanning tree co-registration approach for time-series Sentinel-1 TOPS data," *IEEE J. Sel. Topics Appl. Earth Observ. Remote Sens.*, vol. 12, no. 8, pp. 3004–3013, Aug. 2019.

[18] C. Zhao, Z. Li, P. Zhang, B. Tian, and S. Gao, "Improved maximum likelihood estimation for optimal phase history retrieval of distributed scatterers in insar stacks," *IEEE Access*, vol. 7, pp. 186319–186327, 2019.

[19] G. Fornaro, S. Verde, D. Reale, and A. Pauciullo, "CAESAR: An approach based on covariance matrix decomposition to improve multibaseline–multitemporal interferometric SAR processing," *IEEE Trans. Geosci. Remote Sens.*, vol. 53, no. 4, pp. 2050–2065, Apr. 2015.

[20] N. Cao, H. Lee, and H. C. Jung, "A phase-decomposition-based PSInSAR processing method," *IEEE Trans. Geosci. Remote Sens.*, vol. 54, no. 2, pp. 1074–1090, Feb. 2016.

[21] H. Ansari, F. De Zan, and R. Bamler, "Sequential estimator: Toward efficient InSAR time series analysis," *IEEE Trans. Geosci. Remote Sens.*, vol. 55, no. 10, pp. 5637–5652, Oct. 2017.

[22] S. Samiei-Esfahany, J. E. Martins, F. van Leijen, and R. F. Hanssen, "Phase estimation for distributed scatterers in InSAR stacks using integer least squares estimation," *IEEE Trans. Geosci. Remote Sens.*, vol. 54, no. 10, pp. 5671–5687, Oct. 2016.

[23] S. S. Esfahany, "Exploitation of distributed scatterers in synthetic aperture radar interferometry," 2017.

[24] C. Ning, L. Hyongki, and J. Hahn Chul, "Mathematical framework for phase-triangulation algorithms in distributed-scatterer interferometry," *IEEE Geosci. Remote Sens. Lett.*, vol. 12, no. 9, pp. 1838–1842, Sep. 2015.

[25] B. Zhang, R. Wang, Y. Deng, P. Ma, H. Lin, and J. Wang, "Mapping the yellow river delta land subsidence with multitemporal SAR interferometry by exploiting both persistent and distributed scatterers," *ISPRS-J. Photogramm. Remote Sens.*, vol. 148, pp. 157–173, 2019.

[26] Z. Zhang, Y. Tang, H. Zhang, and C. Wang, "Phase estimation for distributed scatterer INSAR: A comparison between different methods," in *Proc. 10th Eur. Conf. Synthetic Aperture Radar*, 2014, pp. 1–4.

[27] H. Ansari, F. De Zan, and R. Bamler, "Efficient phase estimation for interferogram stacks," *IEEE Trans. Geosci. Remote Sens.*, vol. 56, no. 7, pp. 4109–4125, Jul. 2018.

[28] C. Zhao, Z. Li, B. Tian, P. Zhang, and Q. Chen, "A ground surface deformation monitoring InSAR method using improved distributed scatterers phase estimation," *IEEE J. Sel. Topics Appl. Earth Observ. Remote Sens.*, vol. 12, no. 11, pp. 4543–4553, Nov. 2019.

[29] X. L. Lv, B. Yazici, M. Zeghal, V. Bennett, and T. Abdoun, "Joint-scatterer processing for time-series InSAR," *IEEE Trans. Geosci. Remote Sens.*, vol. 52, no. 11, pp. 7205–7221, Nov. 2014.

[30] A. Parizzi, and R. Brcic, "Adaptive InSAR stack multilooking exploiting amplitude statistics: A comparison between different techniques and practical results," *IEEE Geosci. Remote Sens. Lett.*, vol. 8, no. 3, pp. 441–445, May 2011.

[31] M. Schmitt, J. L. Schonberger, and U. Stilla, "Adaptive covariance matrix estimation for multi-baseline InSAR data stacks," *IEEE Trans. Geosci. Remote Sens.*, vol. 52, no. 11, pp. 6807–6817, Nov. 2014.

[32] A. Ferretti, A. Fumagalli, F. D. Zan, A. Rucci, and S. Tebaldini, "Process for filtering interferograms obtained from SAR images acquired on the same area," U.S. Patent 8711029, Apr. 29, 2014.

[33] Y. Gao, S. Zhang, T. Li, L. Guo, Q. Chen, and S. Li, "A novel two-step noise reduction approach for interferometric phase images," *Opt. Lasers Eng.*, vol. 121, pp. 1–10, 2019.

[34] Y. Gao, S. Zhang, K. Zhang, and S. Li, "Frequency domain filtering SAR interferometric phase noise using the amended matrix pencil model," *Comput. Model. Eng. Sci.*, vol. 119, no. 2, pp. 349–363, 2019.

[35] S. Li, S. Zhang, Y. Gao, and Q. Zhang, "Slope-compensated interferogram filter with ESPRIT for adaptive frequency estimation," *IET Image Process*, vol. 13, no. 8, pp. 1289–1294, Jun. 2019.

[36] Q. Wang, H. Huang, A. Yu, and Z. Dong, "An efficient and adaptive approach for noise filtering of SAR interferometric phase images," *IEEE Geosci. Remote Sens. Lett.*, vol. 8, no. 6, pp. 1140–1144, Nov. 2011.

[37] M. Jiang, X. L. Ding, R. F. Hanssen, R. Malhotra, and L. Chang, "Fast statistically homogeneous pixel selection for covariance matrix estimation for multitemporal InSAR," *IEEE Trans. Geosci. Remote Sens.*, vol. 53, no. 3, pp. 1213–1224, Mar. 2015.

[38] R. Abdelfattah, and J. M. Nicolas, "Interferometric SAR coherence magnitude estimation using second kind statistics," *IEEE Trans. Geosci. Remote Sens.*, vol. 44, no. 7, pp. 1942–1953, Jul. 2006.

[39] J. S. LEE, and M. R. GRUNES, "Classification of multi-look polarimetric SAR imagery based on complex wishart distribution," *Int. J. Remote Sens.*, vol. 15, pp. 2299–2311, 1994.

[40] Z. Li, W. Zou, X. Ding, Y. Chen, and G. Liu, "A quantitative measure for the quality of InSAR interferograms based on phase differences," *Photogramm. Eng. Remote Sens.*, vol. 70, pp. 1131–1137, 2004.

Shijin Li received the B.S. degree in survey and mapping engineering in 2017 from China University of Mining and Technology, Xuzhou, China, where he is currently working toward the Ph.D. degree in geodesy and surveying engineering at the School of Environment Science and Spatial Informatics.

His current research interests include the fields of interferometric synthetic aperture radar phase filtering, multitemporal InSAR data processing, and deformation measurement.

Shubi Zhang received the B.S. degree in mine surveying in 1987, the M.S. degree in survey and mapping engineering in 1995 and the Ph.D. degree in geodesy and surveying engineering in 2004 from the School of Environment Science and Spatial Informatics, China University of Mining and Technology, Xuzhou, China.

He is currently a Professor with the School of Environment Science and Spatial Informatics, China University of Mining and Technology, Xuzhou, China. His current research interests include modern surveying adjustment and data processing, navigation and positioning, and synthetic aperture radar interferometry applications.
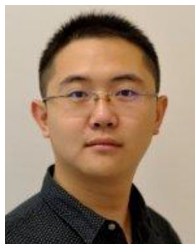
Tao Li received the B.Eng. degree in photogrammetry and remote sensing from the Shandong University of Science and Technology, Shandong, China, in 2009, and the Ph.D. degree from the Southwest Jiaotong University, Chengdu, China, in 2014

He is currently an Associate Research Professor with the Land Satellite Remote Sensing Application Center, MNR, China. His current research interests include InSAR, MTInSAR for mapping the topography and deformation information in China territorial areas.

Qianfu Chen received the B.S. degree in surveying and mapping engineering from Nanjing Normal University, Nanjing, China, in 2012 and the M.S. degree in photogrammetry and remote sensing from Chinese Academy of Surveying and Mapping, Beijing, China, in 2015.

He is currently with the Land Satellite Remote Sensing Application Center, MNR of China, Beijing, China. His research interests include the fields of interferometric calibration, geometric calibration, InSAR data processing, InSAR software development, and SAR applications.

Yandong Gao received the B.S. and M.S. degrees in survey and mapping engineering from University of Science and Technology Liaoning, Anshan, China, in 2013 and 2016, respectively, and the Ph.D. degree in geodesy and surveying engineering from the School of Environment Science and Spatial Informatics, China University of Mining and Technology, Xuzhou, China, in 2019.

He is currently a Post-Doctoral Research Fellow with the School of Environment Science and Spatial Informatics, University of Mining and Technology, Xuzhou, China. His research interests include the fields of interferometric phase filtering, phase unwrapping, and synthetic aperture radar interferometry signal processing and applications.

Xiang Zhang received the B.S. degree in survey and mapping engineering in 2010, the M.S. degree in geodesy and surveying engineering in 2013 and the Ph.D. degree in photogrammetry and remote sensing in 2016 from the School of Environment Science and Spatial Informatics, China University of Mining and Technology, Xuzhou, China.

He is currently an Engineer and an Assistant Research Fellow with the Land Satellite Remote Sensing Application Center, Ministry of Natural Resources of P.R. China. His research interests include the fields of DEM reconstruction and deformation monitoring with InSAR, soil and vegetation parameter retrieval using multisensor SAR data and SAR system specification and simulation analysis.